

Characterization and Erosion Modeling of a Nozzle-Based Inflow-Control Device

Jógvan J. Olsen and Casper S. Hemmingsen, Technical University of Denmark; Line Bergmann, Welltec; Kenny K. Nielsen and Stefan L. Glimberg, Lloyd's Register Consulting—Energy; and Jens H. Walther, Technical University of Denmark

Summary

In the petroleum industry, water-and-gas breakthrough in hydrocarbon reservoirs is a common issue that eventually leads to uneconomic production. To extend the economic production lifetime, inflow-control devices (ICDs) are designed to delay the water-and-gas breakthrough. Because the lifetime of a hydrocarbon reservoir commonly exceeds 20 years and it is a harsh environment, the reliability of the ICDs is vital.

With computational fluid dynamics (CFD), an inclined nozzle-based ICD is characterized in terms of the Reynolds number, discharge coefficient, and geometric variations. The analysis shows that especially the nozzle edges affect the ICD flow characteristics. To apply the results, an equation for the discharge coefficient is proposed.

The Lagrangian particle approach is used to further investigate the ICD. This allows for erosion modeling by injecting sand particles into the system. By altering the geometry and modeling several scenarios while analyzing the erosion in the nozzles and at the nozzle edges, an optimized design for incompressible media is found. With a filleted design and an erosion-resistant material, the mean erosion rate in the nozzles may be reduced by a factor of more than 2,500.

Introduction

It is common to use long horizontal wells to increase reservoir contact and hydrocarbon recovery (Lien et al. 1991). Because horizontal wells typically have a higher production at the heel than at the toe of the well as a result of uneven formation damage and the pressure difference in the long pipe, premature water or gas breakthrough is a common issue (Birchenko et al. 2010; Feng et al. 2012). Eventually, because of the difference in density and viscosity of oil, water, and gas, cresting occurs, severely decreasing hydrocarbon production (Joshi 1991). Placing ICDs along the completion introduces a passively controlled pressure drop, and can result in a more uniform influx along the completion. This can significantly delay the cresting, and gives a potential for a higher reservoir recovery. Fig. 1 illustrates how ICDs can extend reservoir lifetime compared with openhole completions.

Because a hydrocarbon reservoir is typically in production for 5 to > 20 years (Garcia et al. 2009), the longtime reliability of the completion is important. Most ICDs have to be set to introduce the correct pressure drop before entering the well. Therefore, it is important that they can maintain their planned characteristics, because repairing or interchanging components in a well is often not a viable option. In particular, erosion and plugging can lead to the deviation of the planned inflow profile (Visosky et al. 2007; Garcia et al. 2009). Because nozzle-based ICDs are prone to erosion (Zeng et al. 2013), their performance has to be known for a large range of scenarios to ensure that the planned inflow characteristics will be maintained throughout the entire reservoir lifetime. The current research on erosion of ICDs is outlined by Greci et al. (2014). They found five examples of experimental research in which three experiments showed less than 6% change in pres-

sure drop, and two experiments showed no change. No previous research was found that showed erosion in ICDs analyzed by use of numerically simulated particles.

To prevent erosion from occurring in the ICDs, large particles are filtered upstream from the flow with sand screens. When investigating erosion, the primary erosion factors are particle size, particle concentration, particle shape, particle velocity, angle of impact, and wall material (Coronado et al. 2009; Oka et al. 2009). For the present case, sand-particle sizes 100 to 1000 μm in diameter are investigated. The larger particles can penetrate the sand screen initially, whereas only the smaller particles will pass through after a natural sandpack has built up on the sand screen (Feng et al. 2012). In addition, Zamberi et al. (2014) show that sand-screen erosion can occur, allowing the large sand particles to pass through.

The nozzle-based ICDs have been deployed in wells since 2015, for operators in West Africa and operators in the Middle East. The applications have been different: Some were installed to use the ICDs in the application as gas lift valve and some in the application as zonal-production valve. Since the end of 2016, more than 35 ICDs have been installed and used in wells, and more than 250 valves have been ordered. The objective of this paper is to use numerical methods to characterize and investigate erosion for a nozzle-based ICD with varying geometry. The purpose is to optimize the ICD in terms of erosion to improve long-time performance and to present the results with simple equations ready to implement in reservoir simulators.

CFD Formulation

With CFD, the ICD can be analyzed for a range of scenarios by spatially discretizing the domain and solving the fundamental fluid-dynamics equations. This allows for numerically analyzing the ICD in terms of flow characteristics and erosion rates.

Fundamental Equations for Incompressible Flow. The governing equations for solving the flow are the Navier-Stokes and continuity equations. Because the maximum simulated pressure difference will be $\Delta p = 20$ bar, gas release and viscosity changes are assumed negligible. In addition, with data from Lien et al. (1991), the change in density is only 1.7 kg/m^3 (0.2%) at $\Delta p = 20$ bar, meaning the oil can be assumed incompressible. To save computational time, the steady-state solution can be found. The governing equations are modeled by splitting the velocity u_i into a mean (\bar{u}_i) and a fluctuating component (u'_i),

$$u_i = \bar{u}_i + u'_i, \dots \dots \dots (1)$$

here written in Einstein notation.

The mean continuity equation for an incompressible fluid is

$$\frac{\partial \bar{u}_j}{\partial x_j} = 0, \dots \dots \dots (2)$$

where u_j is the velocity vector and x_j denotes the spatial coordinate.

The incompressible time-averaged Navier-Stokes equation (White 2006) for solving the fluid momentum is

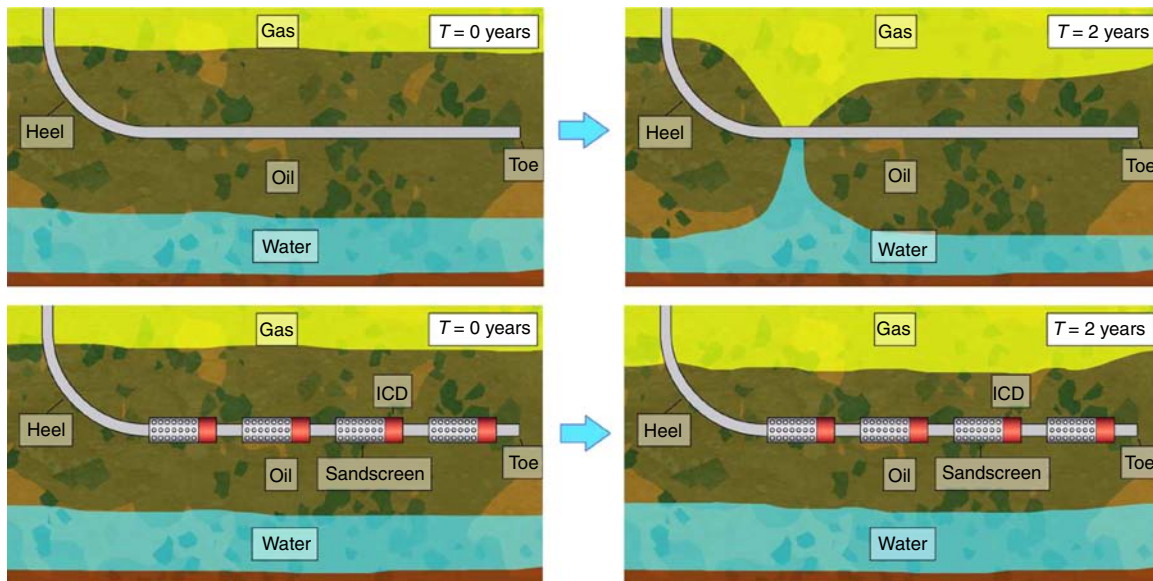


Fig. 1—Inflow-control devices (ICDs) can delay water/gas breakthrough, thereby extending reservoir lifetime. The two upper images show the cresting effect potentially occurring when using an openhole completion, and the bottom two images show the effect of even oil influx obtained with ICDs. Modified from Olsen (2015).

$$\rho \bar{u}_j \frac{\partial \bar{u}_i}{\partial x_j} = \frac{\partial}{\partial x_j} \left[-\bar{p} \delta_{ij} + \mu \left(\frac{\partial \bar{u}_i}{\partial x_j} + \frac{\partial \bar{u}_j}{\partial x_i} \right) - \bar{\tau}_{ij} \right], \dots \dots \dots (3)$$

where ρ is the density, p is the pressure, δ_{ij} is the Kronecker delta, μ is the dynamic viscosity, and $\bar{\tau}_{ij} = \overline{\rho u_i' u_j'}$ is the Reynolds stress term. Because only the mean flow properties will be referenced, the bar symbol is removed in future notation.

To provide closure, the Reynolds stress is modeled with Reynolds-averaged Navier-Stokes (RANS) equations. Three turbulence models will be used: The two-equation realizable $k-\epsilon$ model (Shih et al. 1995), the two-equation shear-stress transport (SST) $k-\omega$ model (Menter 1994), and the one-equation Spalart-Allmaras model (Spalart and Allmaras 1994). Because turbulence theory is a very large and complex field, we refer to Wilcox (1994) for further discussions.

Lagrangian Multiphase Formulation. To solve particle motion, the Lagrangian formulation is used. Here, the sand grains are modeled as parcels, in which each parcel represents multiple sand grains with a given density, diameter, and position. Instead of modeling every particle, parcels allow for a statistical approach with which it is necessary to model only a sufficient number of parcels. The number of parcels required depends on the flow field and geometry. The flow is assumed dilute, meaning particle/particle interactions are neglected for the present case (Elghobashi 1994). In addition, the Lagrangian formulation is limited to non-rotating particles with a constant shape.

Because the sand particles used in the Lagrangian multiphase model will have significant mass, they are modeled as solid particles. The conservation of momentum is for a solid particle defined as

$$m_p \frac{dv_{p,i}}{dt} = F_{d,i} + F_{p,i} + F_{vm,i} + F_{SL,i} + F_{g,i}, \dots \dots \dots (4)$$

where m_p is the mass of the particle, $v_{p,i}$ is the velocity of the particle, $F_{d,i}$ is the drag force defined with the Schiller-Naumann correlation (Schiller and Naumann 1933), $F_{p,i}$ is the pressure-gradient force provided by CD-adapco (2015), $F_{vm,i}$ is the virtual mass force provided by CD-adapco (2015) in which the virtual mass coefficient is set to $C_{vm} = 0.5$, $F_{SL,i}$ is the shear lift force modeled by use of Sommerfeld (2000), and $F_{g,i}$ is the gravity force.

The turbulent-dispersion model (CD-adapco 2015) is used to account for the effects that the turbulent eddies have on the par-

ticles, because the turbulent eddies are not resolved when using a RANS model.

To calculate the particle trajectory after impacting a wall, the particle-restitution coefficients are set for the normal restitution coefficient (NRC) and the tangential restitution coefficient (TRC). For steel oilfield control valves, Forder et al. (1998) propose the following coefficients:

$$NRC = 0.988 - 0.78\beta + 0.19\beta^2 - 0.024\beta^3 + 0.027\beta^4, \dots \dots \dots (5)$$

$$TRC = 1 - 0.78\beta + 0.84\tau^2 - 0.21\beta^3 + 0.028\beta^4 - 0.022\beta^5, \dots \dots \dots (6)$$

where β is the particle-incidence angle. The exact restitution coefficients are not considered as vital if the particles only affect the nozzle walls once.

Erosion Model. When modeling erosion, the erosion rate on a solid-surface element, E_f , is defined as the amount of mass eroded from a face area over time:

$$E_f = \frac{1}{A_f} \sum_{\pi(f)} \dot{m}_\pi e_r, \dots \dots \dots (7)$$

where A_f is the face area, \dot{m}_π is the impacting parcel mass flow rate, and e_r is the user-defined volumetric erosion rate per mass of particles dependent on the correlation used. The summation over $\pi(f)$ means that the sum of parcels impacting the face is used. The total eroded mass can thus be found by calculating the surface integral of Eq. 7:

$$E_t = \int_S E_f dS. \dots \dots \dots (8)$$

The mean erosion rate is calculated as the total erosion rate divided by the density of the wall material and the surface area of the nozzle:

$$E_m = \frac{E_t}{\rho_{\text{wall}} A_{\text{surf}}}. \dots \dots \dots (9)$$

For defining the volumetric erosion rate per mass of particles, Boye (2015) showed that the Oka correlation (Oka et al. 2009) is the most accurate for the modeling of erosion caused by sand particles in water. The formulation is

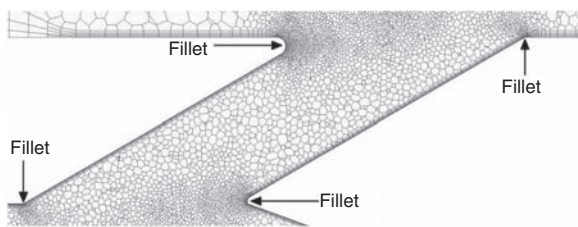


Fig. 4—Cross section of the 4.1-million-cell mesh. Heavy refinements are applied to the nozzle edge and fillet. The arrows mark the edges that are rounded. All fillets are the same size.

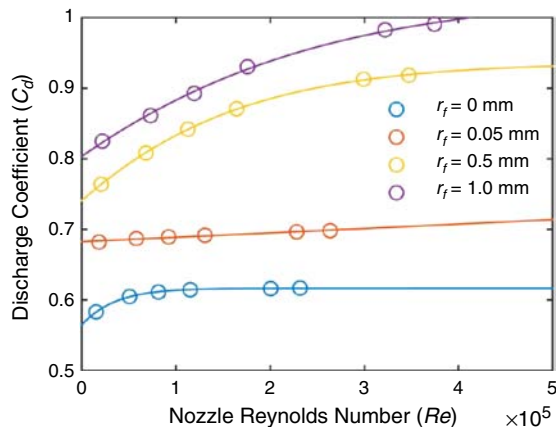


Fig. 6—Discharge coefficient for varying geometries, where r_f is the fillet radius. $r_f = 0$ mm represents a sharp-edged nozzle. The points represent data from the CFD simulations, and the lines represent the fitted curve with Eq. 15.

mesh-independent solution; see Olsen (2015) for details. The mesh providing a mesh-independent solution can be seen in Fig. 4. An overview of the flow can be seen in Fig. 5. The figure illustrates that a small region of the nozzle has high velocity, and flow separation is observed downstream of the nozzle edge. Fig. 6 shows that, for all fillet radii, C_d converges toward a constant value for high Reynolds numbers. Fig. 6 also shows that the fillet radius has a significant impact on the discharge coefficient. Furthermore, Fig. 6 demonstrates that the larger the fillet, the more variable the C_d is. This means that, for large fillets, the ICD becomes increasingly sensitive to changes in viscosity, which is in contrast to Eq. 14.

To calculate the ICD discharge coefficient, the following equation is proposed:

$$C_d = \frac{c_1}{e^{c_2 Re} + c_3}, \dots \dots \dots (15)$$

where the fitted coefficients are shown in Table 1. Fig. 6 shows that the proposed equation gives a good fit. Eq. 15 shows that C_d always will have an asymptotic value, c_1/c_3 , for large Reynolds number (Re).

Erosion Modeling

The previous section showed that minor changes to the nozzle fillet radii do have a significant impact on the ICD characteristics.

| | |
|-----------------------|----------------------------------|
| $n_1 = 0.8004$ | $n_2 = 1.0733$ |
| $k_1 = 2.3761$ | $k_2 = 0.1900$ |
| $v_{ref} = 104.0$ m/s | $d_{ref} = 3.26 \cdot 10^{-4}$ m |

Table 2—Coefficients for Oka correlation (Oka et al. 2009). From Olsen (2015).

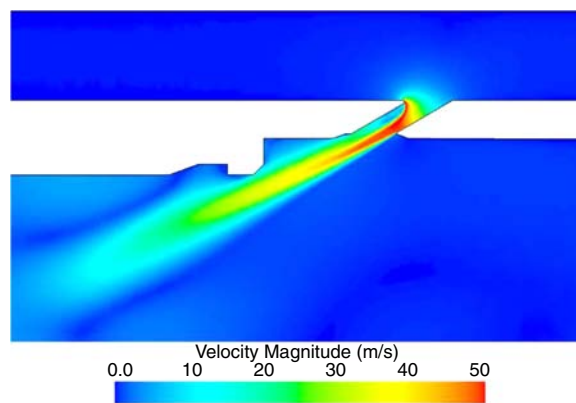


Fig. 5—Overview of the flow with the 0.5-mm fillet radius and $\Delta p = 10$ bar.

| Fillet Radii | c_1 | c_2 | c_3 |
|-----------------|--------|-------------------------|--------|
| $r_f = 0.00$ mm | 6.7625 | $-3.0006 \cdot 10^{-5}$ | 10.967 |
| $r_f = 0.05$ mm | 3.6004 | $-4.9686 \cdot 10^{-7}$ | 4.2746 |
| $r_f = 0.50$ mm | 3.5349 | $-7.5090 \cdot 10^{-6}$ | 3.7705 |
| $r_f = 1.00$ mm | 3.6077 | $-5.1749 \cdot 10^{-6}$ | 3.4893 |

Table 1—Fitting coefficients to be used in Eq. 15.

In combination with the long lifetime of a reservoir, minor changes to the geometry can have a large impact on the overall reservoir performance. By performing a series of erosion analyses for varying scenarios and optimizing the ICD on the basis of the results, improved performance can be achieved.

The manufacturer is aware of erosion as an important issue for nozzle-based ICDs, and is therefore using erosion-resistant inserts for their nozzles. To quantify the difference in materials, the results will be analyzed with both tungsten carbide and carbon steel as wall materials, because these two materials are already used by the manufacturer. The erosion resistance for both materials is found in Haugen et al. (1995), and the density is provided from the manufacturer, $\rho_{steel} = 8200$ kg/m³ and $\rho_{tungsten} = 19,600$ kg/m³.

The default scenario will be the same as in the preceding section, and the same physics and boundary conditions are applied. In addition, the sand mass flow rate is found from Garcia et al. (2009) to be $\dot{m}_{sand} = 2.9 \cdot 10^{-6}$ kg/s at the wellbore inlet on each side. Eq. 7 shows that the erosion rate depends linearly on the sand mass flow rate, meaning that the results are easily scalable-dependent on the expected sand-production rate for a specific reservoir.

The particle diameter is set as default to be $d_p = 250$ μm, which Haugen et al. (1995) show is the typical sand size for North Sea reservoirs. The particle density is set to $\rho_{sand} = 2650$ kg/m³ equal to sand density used in the erosion experiment by Zhang et al. (2007), which was also used as a validation case in the work by Boye (2015).

For evaluating erosion on the walls, the appropriate constants for the Oka correlation (Eq. 10) are found from the experiment by Zhang et al. (2007) and are listed in Table 2. When using either steel or tungsten carbide, the wall density, volumetric erosion rate per mass of particles, and Vickers hardness, H_v , must be set to their respective values listed in Table 3.

The flow is modeled in steady state with the realizable $k-\epsilon$ turbulence model (Shih et al. 1995). After convergence is reached, the parcels are injected with a maximum residence time of 100 seconds. To ensure accurate comparison between different scenarios, 1.5 million parcels are injected 10 mm from the wellbore

| Material | e_{90} | H_v | ρ_{wall} |
|----------|--|-----------|-------------------------|
| Steel | $1.76 \cdot 10^{-3} \text{ m}^3/\text{kg}$ | 2.354 GPa | 8200 kg/m ³ |
| Tungsten | $2.40 \cdot 10^{-5} \text{ m}^3/\text{kg}$ | 17.65 GPa | 19600 kg/m ³ |

Table 3—Wall-material properties. From Olsen (2015).

inlets with an equidistant spacing between each parcel. Furthermore, a new mesh-independence analysis is performed for the erosion analysis to ensure a mesh-independent solution, which resulted in a mesh containing 16.0 million cells; see Olsen (2015) for details.

Erosion Results. The erosion aspects are analyzed by investigating the erosion pattern and the mean erosion rate in the nozzles. To ensure an accurate mean, the results from all four nozzles are used when discussing the mean erosion rate.

Fig. 7a shows the initial results for the default scenario with steel nozzles. The erosion results demonstrate that there is a localized erosion at the center of the nozzles. Fig. 8 shows the tangential in-plane velocity contours and the location of the particles with the sharp-edged nozzle; see Fig. 9 for reference coordinate system. The results show strong secondary flow structures in the entrance of the nozzle, contributing to the displacement of the particles toward the wall. By minimizing the separation, the strength of the secondary flow should decrease, lowering the ero-

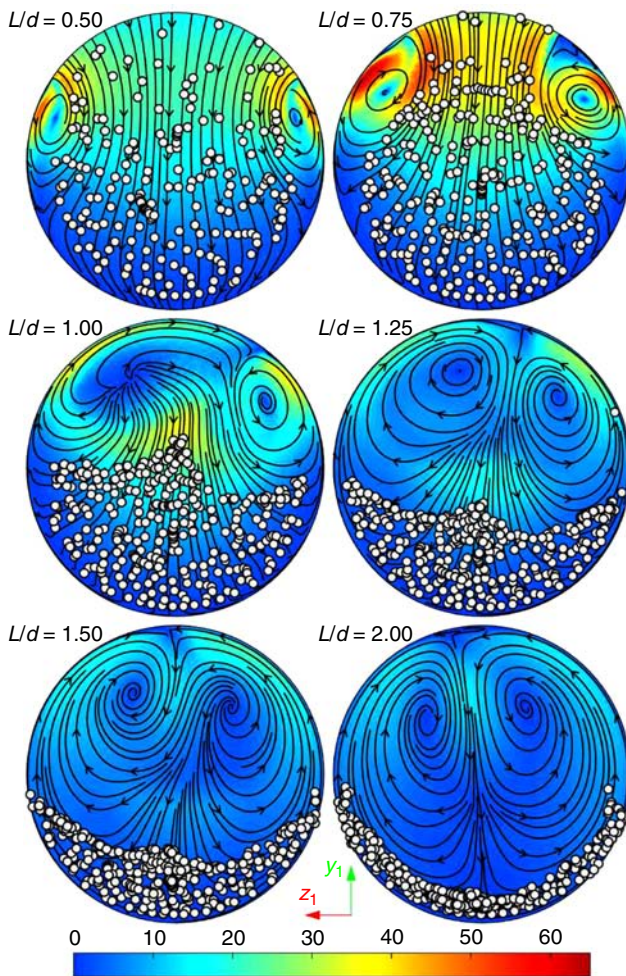


Fig. 8—Tangential velocity contour (m/s) in the $[x_1, y_1, z_1]$ coordinate system for the sharp-edged nozzle. The white circles represent the particle position. The high-velocity secondary flows pull the particles toward the nozzle edge, causing erosion.

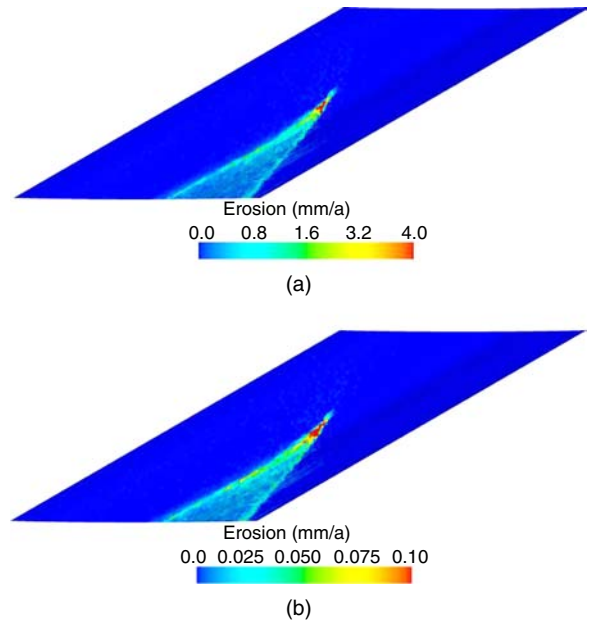


Fig. 7—Close-up view of the nozzle erosion rate with steel (a) and tungsten carbide (b), respectively. Notice the change in scale. The mean erosions for the nozzles were $E_{m,steel} = 0.47 \text{ mm/a}$ and $E_{m,tungsten} = 0.016 \text{ mm/a}$.

rosion rate. The figure also shows that the secondary flows are not symmetric until after $L/d = 2$, meaning that the erosion is not entirely symmetrical. In addition, Fig. 8 shows that the particles are densely packed when impacting the nozzle wall. This might interfere locally with the dilute assumption, and can be a source of inaccuracy leading to overestimated erosion rates because some particles do not collide with the wall but with each other, which is not modeled.

Because the predicted mean erosion rate is $E_{m,steel} = 0.47 \text{ mm/a}$, optimizing the nozzles is important if the planned inflow characteristics should be maintained. With the assumption that the pressure drop should not change more than 5%, the simulated ICD lifetime will be less than 6 months.

Fig. 7b shows the erosion with tungsten carbide. Comparing the mean erosion rate for the two materials gives a factor of 29 in difference, which equals a lifetime of 14 years. The figure shows a very similar erosion pattern for the two materials. Fig. 10 shows the particle-impact angle. It is observed that 95% of the particles have an impact angle less than 12.5° . The nearly identical erosion pattern is a result of the normalized $g(\beta)$ shown in Fig. 2 being nearly identical for the two materials at low angles. Furthermore, this shows that, if further erosion resistance should be achieved, a material resistant to the cutting action should be found.

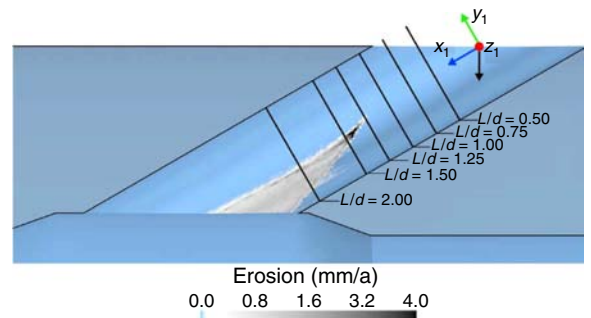


Fig. 9—Position of local coordinate system and velocity planes. The local coordinate-system origin is placed at the center of the nozzle inlet with x_1 parallel to the nozzle. L is the position down the x_1 -axis, and d is the nozzle diameter. The black arrow represents the view direction in Fig. 18.

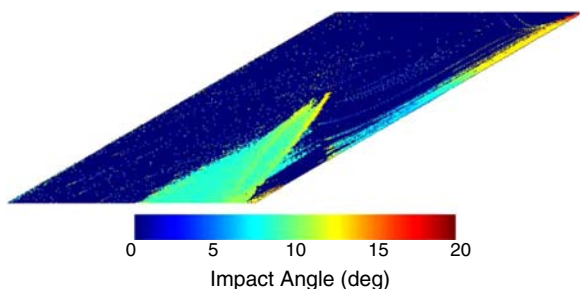


Fig. 10—Particle-impact angle in the nozzle. The mean particle-impact angle is 9.4° . 95% of the particles have an impact angle $<12.5^\circ$. Zero impact angle represents regions where no particle impacts are observed.

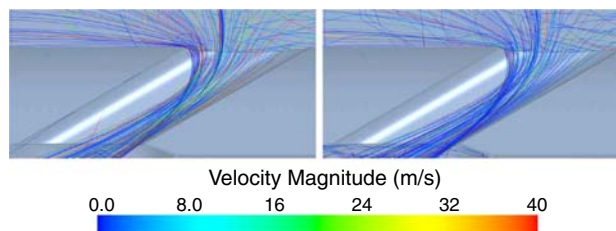


Fig. 12—Particle trajectory in the nozzle. The turbulent-dispersion model is activated on the right image. The particle trajectory can be seen to be only slightly wider when the turbulent dispersion is activated. From Olsen (2015).

The nozzle edge is also investigated. It shows that the erosion rates were exceeding 0.1 mm/a and 4.0 mm/a at several locations on the nozzle edge for tungsten carbide and steel, respectively. This means that, after only a short time, flow characteristics of the nozzles will change.

Because using tungsten-carbide nozzles gives a large improvement in comparison to steel nozzles, the remaining erosion simulations will be made with tungsten carbide as wall material.

Sensitivity to Turbulence Models. Because the behavior of the separation in the nozzle is highly influenced by the choice of turbulence model, three standard turbulence models are compared in terms of erosion rate. Fig. 11 shows the erosion prediction for the realizable $k-\varepsilon$ model, the Spalart-Allmaras model, and the $k-\omega$ SST model. The figure shows that the realizable $k-\varepsilon$ model has a much sharper erosion pattern in comparison with the two other turbulence models. It is noticed that the Spalart-Allmaras model and the $k-\omega$ SST model show similar erosion patterns. Because of the uncertainties associated with erosion modeling and the lack of experimental work for inclined nozzles, no conclusions can be made on which model performs best. The two largest uncertainties come from imperfect solutions to the flow field, resulting in the particle trajectory being incorrect and in the uncertainty of the erosion-model coefficients. In the validation case by Zhang et al. (2007), they found the deviation in erosion to be 0–25% with water. Because the computational mesh is significantly finer for the present case, the deviation can thus not be expected to exceed 25%.

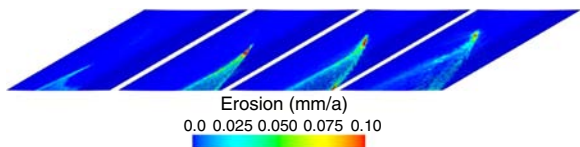


Fig. 14—Particle size used from left to right: 100, 250, 500, and $1000 \mu\text{m}$. The mean erosion rate is $E_{m,100 \mu\text{m}} = 0.0016 \text{ mm/a}$, $E_{m,250 \mu\text{m}} = 0.016 \text{ mm/a}$, $E_{m,500 \mu\text{m}} = 0.031 \text{ mm/a}$, and $E_{m,1000 \mu\text{m}} = 0.019 \text{ mm/a}$. The material is tungsten carbide without the turbulent-dispersion model.

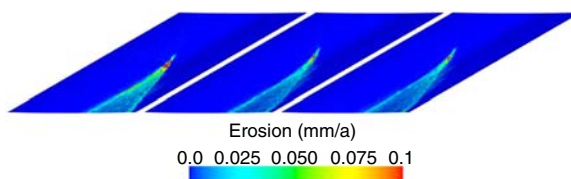


Fig. 11—Turbulence models used from left to right: the realizable $k-\varepsilon$ model, the Spalart-Allmaras model, and the $k-\omega$ SST model. The mean erosion is $E_{m,k-\varepsilon} = 0.016 \text{ mm/a}$, $E_{m,S-A} = 0.013 \text{ mm/a}$, and $E_{m,k-\omega} = 0.012 \text{ mm/a}$. The material is tungsten carbide.

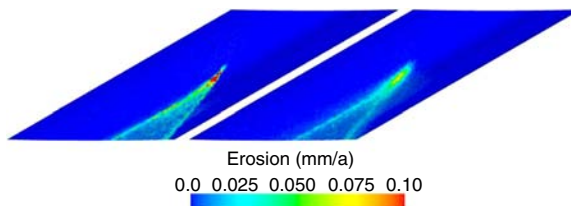


Fig. 13—Comparison of the erosion pattern without (left) and with (right) turbulent dispersion. The patterns are very similar except that the turbulent-dispersion model results in a more-diffused erosion pattern. The mean erosion rates are $E_{m,\text{default}} = 0.016 \text{ mm/a}$ and $E_{m,\text{turbulent}} = 0.016 \text{ mm/a}$. The maximum erosion is lower with the turbulent-dispersion model, because fewer particles affect the exact same location on the wall. The material is tungsten carbide.

To model the effect of turbulent fluctuation on the particle trajectory, the turbulent-dispersion model is used. Activating the turbulent-dispersion model results in the parcel trajectory becoming more chaotic downstream of the nozzles. It is contrary that the particle trajectory before entering the nozzles is very similar, indicating few flow fluctuations in the wellbore. The parcel trajectory in the nozzles (Fig. 12) shows that the behavior is similar with and without turbulent dispersion. Because erosion is only expected in the nozzle wall and nozzle edges, the turbulent-dispersion model can therefore only be expected to have a minor impact on the mean erosion rate.

Fig. 13 shows the erosion pattern with the turbulent-dispersion model. The erosion pattern becomes more diffused when turbulent dispersion is activated, but there is only a 2.5% difference in mean erosion rate. In terms of usability, it is more attractive to run the simulations without turbulent dispersion, because a clear erosion pattern is preferred for analysis. In addition, the turbulent-dispersion model increases the simulation time by more than a factor of 2. Therefore, the turbulent-dispersion model will not be used for the remaining simulations.

Parametric Analysis of Eroding Factors. The type of sand screen used will vary depending on the specific reservoir because the sand-grain size is reservoir-dependent. Therefore, simulations are performed with the particle-grain sizes of 100, 250, 500, and $1000 \mu\text{m}$ in diameter. Fig. 14 demonstrates that the larger the particles are, the higher up the nozzle the erosion starts. Furthermore, almost no erosion can be observed for very small particles. Notice that the erosion rate does not necessarily increase with the particle-grain size, but does instead have a maximum erosion rate when using $500\text{-}\mu\text{m}$ particles. This must be because of the larger particles impacting the nozzles at either small angles or large angles, resulting in lower erosion rates; see Fig. 2.

To investigate how the erosion will vary for different flow velocities, the pressure difference across the nozzle is varied. Fig. 15 shows the erosion for $\Delta p = 5 \text{ bar}$, $\Delta p = 10 \text{ bar}$, and $\Delta p = 20 \text{ bar}$. Notice that the erosion pattern has a similar shape for the three cases. The difference is that, for larger Δp , the erosion rate is higher and starts higher up the nozzle. This indicates that the secondary flows behave identically for all three cases, with the

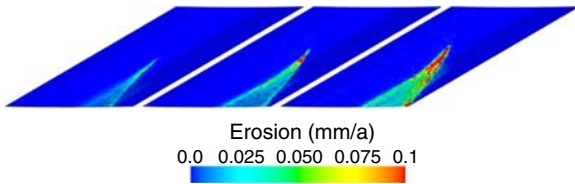


Fig. 15—Pressure difference Δp used from left to right: 5, 10 (default), and 20 bar. The mean erosion is $E_{m, 5 \text{ bar}} = 0.0045 \text{ mm/a}$, $E_{m, 10 \text{ bar}} = 0.016 \text{ mm/a}$, and $E_{m, 20 \text{ bar}} = 0.050 \text{ mm/a}$. The material is tungsten carbide without the turbulent-dispersion model.

difference being that they have different strengths. To investigate this phenomenon, the tangential in-plane velocity contour is investigated. **Fig. 16** shows the secondary flow at $L/d=0.75$ and $L/d=1.25$ for the three pressure variations. The figure shows that the velocity contour is very similar for all cases, creating a nearly identical erosion pattern.

Because the pressure difference from the reservoir to the well varies during the reservoir lifetime, the erosion rate must be known for all relevant pressure differences. For the present case, the following equation is proposed for finding the erosion rate as a function of pressure difference:

$$E_m(\Delta p) = a_1 \Delta p^{a_2}, \dots \dots \dots (16)$$

where the coefficients are $a_1 = 2.15 \cdot 10^{-12}$, $a_2 = 1.65$. **Fig. 17** shows that the proposed equation gives a good fit for the conditions modeled. The proposed equation can be used in near-well nodal simulators described by Johansen and Khoriakov (2007) to model the erosion during the reservoir lifetime. This can give significant information on how the completion characteristics will change during the reservoir lifetime, and might therefore reduce intervention work.

Because the separation in the nozzles is a determining factor in erosion, the nozzle angles are varied and simulated. The results show that the mean erosion rates for the 60° and 90° inclined nozzles are extremely low, $E_{m,60 \text{ deg}} = 0.45 \cdot 10^{-4} \text{ mm/a}$ and $E_{m,90 \text{ deg}} = 0.00 \text{ mm/a}$. Investigating the edges of the nozzles shows significant erosion in both cases; see **Fig. 18**. Therefore, even though the nozzles will not erode for higher nozzle angles, the characteristics will vary during ICD lifetime because the nozzle edge is very prone to erosion.

Optimizing the Nozzle Geometry With Fillets. With the separation in the nozzles identified as the primary erosion mechanism, the nozzle can be optimized by minimizing or removing the separation with fillets.

We considered three cases: $r_f = [0.05 \text{ mm}, 0.50 \text{ mm}, 1.00 \text{ mm}]$. Comparing the tangential velocity field for a $r_f = 0.50\text{-mm}$ filleted nozzle (**Fig. 19**) to that of a sharp-edged nozzle (**Fig. 8**) shows

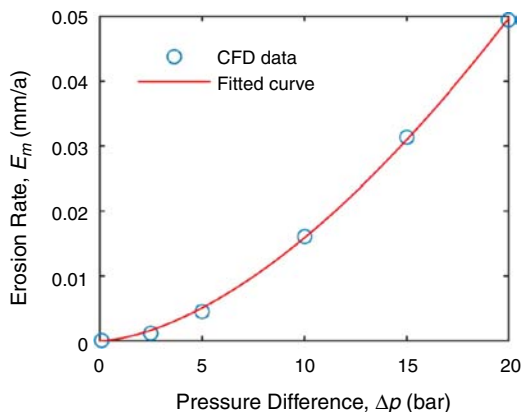


Fig. 17—Erosion rate as a function of pressure difference for the ICD with four 30° inclined nozzles. The material is tungsten carbide.

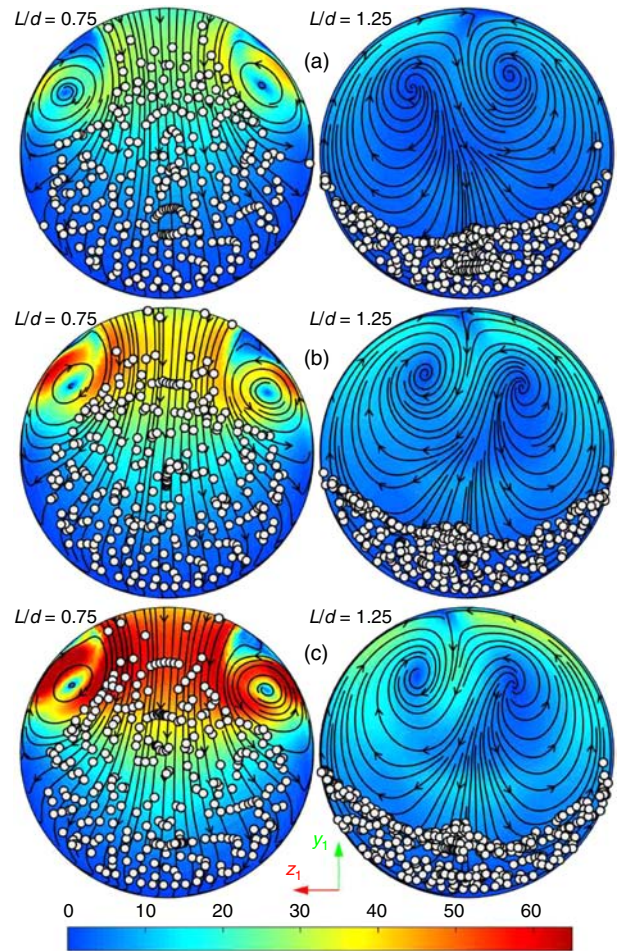


Fig. 16—Tangential velocity contour projected on the z_1 - y_1 plane. Δp is 5, 10, and 20 bar for (a), (b), (c), respectively. It can be seen that, for all three pressure variations, the behavior of the secondary flows is very similar.

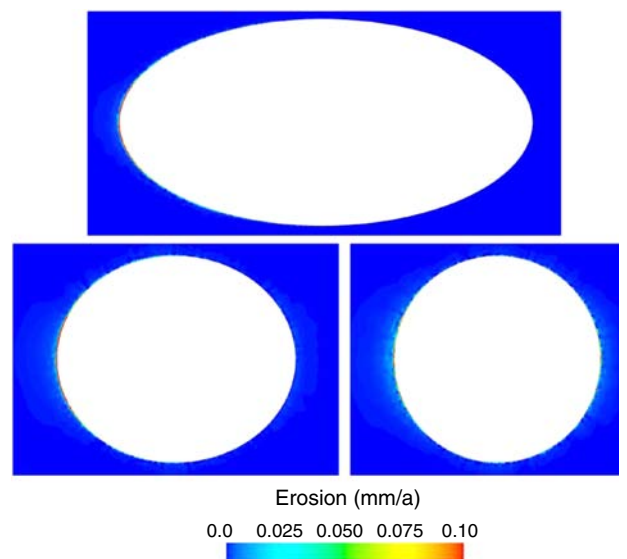


Fig. 18—The nozzle edge seen from the top with varying nozzle angle; refer to Fig. 9. The top image is for a 30° nozzle angle (default). The bottom left and right images are for 60° and 90° nozzle angle, respectively. The material is tungsten carbide without the turbulent-dispersion model.

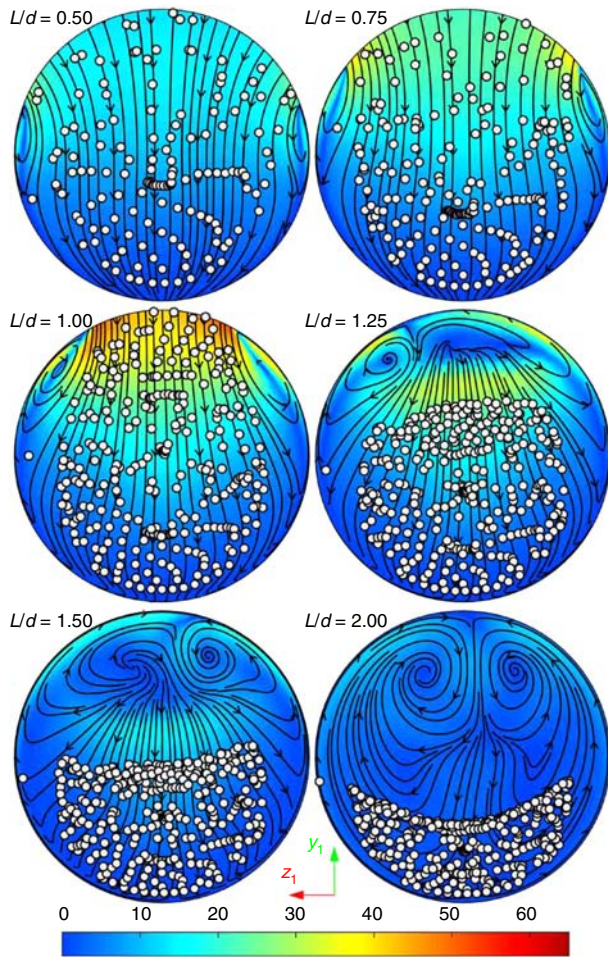


Fig. 19—Tangential velocity contour (m/s) in the $[x_1, y_1, z_1]$ coordinate system for the 0.5-mm filleted nozzle. After decreasing the strength of the separation, fewer particles are seen to move toward the wall.

that the fillets greatly reduce the secondary flows, resulting in less displacement of the particles toward the wall and, hence, less erosion. In addition, this implies that the erosion rate will decelerate over time for the sharp-edged nozzle.

The erosion pattern can be seen in **Fig. 20**. For the $r_f = 0.05$ -mm fillet, a minor improvement is seen because the mean erosion rate has decreased from $E_{m,sharp} = 0.016$ mm/a to $E_{m,rf\ 005} = 0.011$ mm/a. Using fillets that are either $r_f = 0.50$ mm or $r_f = 1.00$ mm shows a major improvement with the mean erosion rate as $E_{m,rf\ 050} = 1.8 \cdot 10^{-4}$ mm/a and $E_{m,rf\ 100} = 2.1 \cdot 10^{-4}$ mm/a, respectively. This means that, according to the simulations, a reduction factor of 89 in erosion rate can be achieved with 0.5-mm fillets.

By applying the erosion-resistant tungsten carbide and using a 0.5-mm fillet on the nozzle edges, a reduction factor of 2,612 in erosion rate is simulated in comparison to the standard sharp-edged steel nozzle. This may increase significantly the accuracy of the flow characteristics during the reservoir lifetime, because the modeled ICD lifetime is now 1,235 years at $\Delta p = 10$ bar. With Eq. 16, this could be translated into 20 years, operating at $\Delta p = 123.5$ bar.

Conclusions

This work has demonstrated how numerical simulations can be used to

- Characterize an ICD in terms of the Reynolds number, discharge coefficient, and fillet radii.
- Investigate erosion parameters and optimize an ICD with CFD by applying erosion-resistant materials and altering the nozzle-edge geometry, resulting in a simulated reduction in mean erosion by a factor of 29 and a factor of 89, respectively. Applying

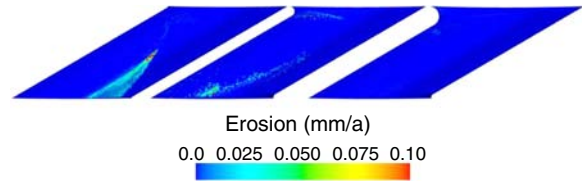


Fig. 20—Fillet radius used from left to right: 0.05, 0.50, and 1.00 mm. The mean erosion is $E_{m,rf\ 005} = 0.011$ mm/a, $E_{m,rf\ 050} = 1.8 \cdot 10^{-4}$ mm/a, and $E_{m,rf\ 100} = 2.1 \cdot 10^{-4}$ mm/a. The material is tungsten carbide without the turbulent-dispersion model.

both methods is modeled to reduce the mean erosion rate by a factor of 2,612, potentially resulting in an ICD lifetime exceeding the reservoir lifetime.

- Systematically analyze characteristics and erosion rates to propose empirical equations to implement in reservoir simulators. This work also shows that the lack of experimental data for eroding nozzles means it cannot be concluded which model is best suited for erosion modeling. The following is recommended for further research:
- Investigate the effect of compressibility in combination with erosion rate and erosion pattern. This topic is particularly relevant for cases in which gas is present in the reservoir.
- Model erosion of other common types of ICDs.
- Model the empirical equations with a nodal approach [see Johansen and Khoriakov (2007)] or near-well simulators to investigate the erosion effects during the reservoir lifetime.

Nomenclature

- a_1, a_2 = fitting coefficients, dimensionless
- A = nozzle area, L^2, m^2
- A_f = face area, L^2, m^2
- A_{surf} = nozzle surface area, L^2, m^2
- c_1, c_2, c_3 = fitting coefficients, dimensionless
- C_d = discharge coefficient, dimensionless
- C_{vm} = virtual mass coefficient, dimensionless
- d = diameter, L, m
- d_n = nozzle diameter, L, m
- d_p = particle diameter, L, m
- d_{ref} = particle-reference diameter, L, m
- E_f = erosion rate on a face, $m/t, kg/s$
- e_r = volumetric erosion rate per mass of particles, $L^3/m, m^3/kg$
- e_{90} = volumetric erosion rate per mass of particles at 90° impact angle, $L^3/m, m^3/kg$
- E_m = mean erosion rate, $L/t, m/s$
- E_t = total eroded mass, $m/t, kg/s$
- F_d = drag force, $cm^3/t^2, kg\ m/s^2$
- F_p = pressure-gradient force, $cm^3/t^2, kg\ m/s^2$
- F_{vm} = virtual-mass force, $cm^3/t^2, kg\ m/s^2$
- F_{SL} = shear-lift force, $cm^3/t^2, kg\ m/s^2$
- F_g = gravity force, $cm^3/t^2, kg\ m/s^2$
- $g(\beta)$ = impact-angle dependence, dimensionless
- H_v = Vickers hardness, $m/L\ t^2, Pa$
- i, j = indices
- k_1, k_2 = constants, dimensionless
- l = characteristic length scale, L, m
- L = length in the x_1 direction, L, m
- \dot{m} = mass flow rate, $m/t, kg/s$
- m_p = particle mass, m, kg
- \dot{m}_π = impacting-parcel mass flow rate, $m/t, kg/s$
- \dot{m}_{prod} = production-well mass flow rate, $m/t, kg/s$
- \dot{m}_{sand} = sand mass flow rate, $m/t, kg/s$
- n = number of nozzles, dimensionless
- n_1, n_2 = constants, dimensionless
- p = pressure, $m/L\ t^2, Pa$
- p_r = restrictive pressure drop, $m/L\ t^2, Pa$
- \bar{p} = mean pressure, $m/L\ t^2, Pa$
- p_{res} = reservoir pressure, $m/L\ t^2, Pa$
- p_w = well pressure, $m/L\ t^2, Pa$

Q = volumetric flow rate, L^3/t , m^3/s
 r_f = fillet radius, where $r_f=0$ is a sharp-edged nozzle, L, m
 r_p = article position, L, m
 r_π = parcel position, L, m
 Re = Reynolds number, dimensionless
 S = surface, L^2 , m^2
 t = time, t, seconds
 T = temperature, T, K
 u = continuum velocity tensor, L/t, m/s
 \bar{u} = mean velocity tensor, L/t, m/s
 u' = fluctuating velocity tensor, L/t, m/s
 u_n = mean nozzle flow velocity, L/t, m/s
 v_p = particle velocity, L/t, m/s
 v_s = particle slip velocity, L/t, m/s
 v_{rel} = particle relative velocity, L/t, m/s
 v_{ref} = particle reference velocity, L/t, m/s
 x_i = spacial tensor, L, m
 β = particle-impact angle, degree
 δ = Kronecker-delta function, dimensionless
 ϵ = turbulent kinetic energy, L^2/t^2 , m^2/s^2
 μ = dynamic viscosity, m/L t, Pa-s
 μ_t = eddy viscosity, m/L t, Pa-s
 ν = kinematic viscosity, L^2/t , m^2/s
 ρ = fluid density, m/L^3 , kg/m^3
 ρ_{sand} = sand density, m/L^3 , kg/m^3
 ρ_{steel} = steel density, m/L^3 , kg/m^3
 $\rho_{tungsten}$ = tungsten density, m/L^3 , kg/m^3
 ρ_{wall} = wall density, m/L^3 , kg/m^3
 π = parcel
 $\bar{\tau}$ = Reynolds stress term, m/Lt^2 , $kg/m \cdot s^2$
 ω = specific dissipation rate, t^{-1} , s^{-1}

Acknowledgments

The authors wish to thank the members of the OPTION (Optimizing Oil Production by Novel Technology Integration) project for their support. The OPTION project is a collaboration between Lloyd's Register Consulting–Energy, Lloyd's Register Senergy, DONG Energy, Welltec, InnovationsFonden–Denmark, Technical University of Denmark, and the University of Copenhagen. The authors wish to acknowledge computational support from the Department of Physics at the Technical University of Denmark.

References

Birchenko, V. M., Muradov, K. M., and Davies, D. R. 2010. Reduction of the Horizontal Well's Heel–Toe Effect With Inflow Control Devices. *Journal of Petroleum Science and Engineering* **75** (1–2): 244–250. <https://doi.org/10.1016/j.petrol.2010.11.013>.
 Boye, R. 2015. *Erosion Modelling of Sand Particles in a Wellbore Using CFD*. BS thesis, Technical University of Denmark.
 CD-adapco. 2015. *User Guide STAR-CCM+ Version 10.02.010*. CD-adapco.
 Coronado, M. P., Garcia, L. A., Russell, R. D. et al. 2009. New Inflow Control Device Reduces Fluid Viscosity Sensitivity and Maintains Erosion Resistance. Presented at the Offshore Technology Conference, Houston, Texas, 4–7 May. OTC-19811-MS. <https://doi.org/10.4043/19811-MS>.
 Elghobashi, S. 1994. On Predicting Particle-Laden Turbulent Flows. *Applied Scientific Research* **52** (4): 309–329. <https://doi.org/10.1007/BF00936835>.
 Feng, Y., Choi, X., Wu, B. et al. 2012. Evaluation of Sand Screen Performance Using a Discrete Element Model. Presented at the SPE Asia Pacific Oil and Gas Conference and Exhibition, Perth, Australia, 22–24 October. SPE-158671-MS. <https://doi.org/10.2118/158671-MS>.
 Forder, A., Thew, M., and Harrison, D. 1998. A Numerical Investigation of Solid Particle Erosion Experienced Within Oilfield Control Valves. *WEAR* **216** (2): 184–193. [https://doi.org/10.1016/S0043-1648\(97\)00217-2](https://doi.org/10.1016/S0043-1648(97)00217-2).
 Garcia, L. A., Coronado, M. P., Russell, R. D. et al. 2009. The First Passive Inflow Control Device That Maximizes Productivity During Ev-

ery Phase of a Well's Life. Presented at the International Petroleum Technology Conference, Doha, Qatar, 7–9 December. IPTC-13863-MS. <https://doi.org/10.2523/IPTC-13863-MS>.
 Greci, S., Least, B., and Tayloe, G. 2014. Testing Results: Erosion Testing Confirms the Reliability of the Fluidic Diode Type Autonomous Inflow Control Device. Presented at the Abu Dhabi International Petroleum Exhibition and Conference, Abu Dhabi, 10–13 November. SPE-172077-MS. <https://doi.org/10.2118/172077-MS>.
 Haugen, K., Kvernfold, O., Ronold, A. et al. 1995. Sand Erosion of Wear-Resistant Materials: Erosion in Choke Valves. *WEAR* **186–187** (1): 179–188. [https://doi.org/10.1016/0043-1648\(95\)07158-X](https://doi.org/10.1016/0043-1648(95)07158-X).
 Johansen, T. E. and Khoriakov, V. 2007. Iterative Techniques in Modeling of Multi-Phase Flow in Advanced Wells and the Near Well Region. *Journal of Petroleum Science and Engineering* **58** (1–2): 49–67. <https://doi.org/10.1016/j.petrol.2006.11.013>.
 Joshi, S. D. 1991. *Horizontal Well Technology*, first edition. Tulsa, Oklahoma: PennWell Publishing Company.
 Lien, S. C., Seines, K., Havig, S. O. et al. 1991. The First Long-Term Horizontal-Well Test in the Troll Thin Oil Zone. *J Pet Technol* **43** (8): 914–973. SPE-20715-PA. <https://doi.org/10.2118/20715-PA>.
 Menter, F. R. 1994. Two-Equation Eddy-Viscosity Turbulence Models for Engineering Applications. *AIAA J.* **32** (8): 1598–1605. <https://doi.org/10.2514/3.12149>.
 Oka, Y., Mihara, S., and Yoshida, T. 2009. Impact-Angle Dependence and Estimation of Erosion Damage to Ceramic Materials Caused by Solid Particle Impact. *WEAR* **267** (1–4): 129–135. <https://doi.org/10.1016/j.wear.2008.12.091>.
 Olsen, J. J. 2015. *Single and Multi-Phase Simulations of Nozzle-Based Inflow Control Devices*. MS thesis, Technical University of Denmark.
 Schiller, L. and Naumann, A. 1933. Über die Grundlegenden Berechnungen bei der Schwerkraftaufbereitung. *Ver. Deutsch. Ing.* **77** (12): 318–320 (in German).
 Shih, T.-H., Liou, W. W., Shabbir, A. et al. 1995. A New $k-\epsilon$ Eddy Viscosity Model for High Reynolds Number Turbulent Flows. *Computers & Fluids* **24** (3): 227–238. [https://doi.org/10.1016/0045-7930\(94\)00032-T](https://doi.org/10.1016/0045-7930(94)00032-T).
 Sommerfeld, M. 2000. Theoretical and Experimental Modelling of Particulate Flows. Technical Report Lecture Series 2000–2006, von Karman Institute for Fluid Dynamics, Belgium.
 Spalart, P. and Allmaras, S. 1994. A One-Equation Turbulence Model for Aerodynamic Flows. *Rech. Aerospatiale* **1**: 5–21. <https://doi.org/10.2514/6.1992-439>.
 Visosky, J. M., Clem, N. J., Coronado, M. P. et al. 2007. Examining Erosion Potential of Various Inflow Control Devices to Determine Duration of Performance. Presented at the SPE Annual Technical Conference, Anaheim, California, 11–14 November. SPE-110667-MS. <https://doi.org/10.2118/110667-MS>.
 White, F. M. 2006. *Viscous Fluid Flow*, third edition, international edition. New York, New York: McGraw-Hill.
 Wilcox, D. C. 1994. *Turbulence Modeling for CFD*, second edition. Glendale, California: DCW Industries, Inc.
 Zamberi, M. S. A., Shaffee, S. N. A., and Jadid, M. et al. 2014. Reduced Erosion of Standalone Sand Screen Completion Using Flow Segmenters. Presented at the Offshore Technology Conference Asia, Kuala Lumpur. SPE-25019-MS. <https://doi.org/10.4043/25019-MS>.
 Zeng, Q., Wang, Z., and Yang, G. 2013. Comparative Study on Passive Inflow Control Devices by Numerical Simulation. *Tech Science Press* **9** (3): 169–180.
 Zhang, Y., Reuterfors, E., McLaury, B. et al. 2007. Comparison of Computed and Measured Particle Velocities and Erosion in Water and Air Flows. *WEAR* **263** (1–6): 330–338. <https://doi.org/10.1016/j.wear.2006.12.048>.

SI Metric Conversion Factors

| | |
|-----------------|-------------|
| cp × 1* | E–03 = Pa·s |
| ft × 3.048* | E–01 = m |
| in. × 2.54* | E+00 = cm |
| psi × 6.894 757 | E+00 = kPa |

*Conversion factor is exact.

Jógvan Juul Olsen is a research assistant at the Technical University of Denmark (TUD), researching in near-well flows by use of computational methods. He holds an MS degree in mechanical engineering from TUD.

Casper S. Hemmingsen is a PhD-degree student at the Department of Mechanical Engineering at TUD. His research area is near-well modeling by use of CFD. Hemmingsen holds BS and MS degrees in fluid mechanics from TUD.

Line Bergmann is an engineer at Welltec A/S. She is responsible for in-house CFD modeling, optimizing products for the completion group. Bergmann holds an MS degree in physics and chemistry from Roskilde University.

Kenny Krogh Nielsen is a team leader and senior principal consultant in the Fluid Dynamics Team at Lloyd's Register Consulting—Energy A/S. He is initiator and chairperson of the board of OPTION JIP, a joint-industry project on improved well and reservoir modeling. Nielsen has 20 years of experience in fluid dynamics, including CFD modeling of single and multi-phase flows within the oil-and-gas industry. He holds a PhD degree in mechanical engineering from Aalborg University

and Texas A&M University and a Post-Graduate Diploma from the von Karman Institute for Fluid Dynamics.

Stefan Lemvig Glimberg is a senior consultant at Lloyd's Register Consulting—Energy A/S. He is the project manager of OPTION JIP, a joint academia/industry project that is bringing front-end research to a level that meets the industry quality requirements. Glimberg's work focuses on computationally efficient and scalable numerical methods with application to oil-and-gas production optimization. He holds an MS degree in computer science from the University of Copenhagen and a PhD degree in applied mathematics from TUD.

Jens H. Walther is a professor of fluid mechanics in the Department of Mechanical Engineering at TUD, and a research associate at the Computational Science and Engineering Laboratory at ETH Zurich, Switzerland. His research areas include the development of high-order Lagrangian methods in CFD, efficient implementation of these methods on modern computer architectures, and the generation and analysis of data through simulations for problems in fluid mechanics. Walther holds a PhD degree in mechanical engineering from TUD.